Modeling of 300 GHz Chip-to-Chip Wireless Channels in Metal Enclosures

Jinbang Fu, Prateek Juyal, and Alenka Zajić *Senior Member, IEEE*
Georgia Institute of Technology, Atlanta, GA 30332 USA

***Abstract*—This paper proposes a two dimensional (2-D) statistical channel model for Terahertz (THz) chip-to-chip wireless communication in desktop size metal enclosures. This model differs from traditional statistical channel models as it models both traveling and resonant waves that exist inside metal enclosures. Based on the cavity environment and the statistical properties of the channel inside the metal cavity, the geometrical model which describes propagation in resonant cavity as a superposition of LoS, single bounced (SB), double bounced (DB), and multi-bounced (MB) rays is proposed. Based on the geometrical model, a parametric reference model is proposed. Furthermore, the path loss model that captures signal strength variation in a resonant cavity is proposed. Frequency correlation functions (FCF) and power delay profiles (PDP) for different possible chip-to-chip communication scenarios are derived and compared with the measured ones. The results show a good agreement between the simulated and measured statistics.**

***Index Terms*—Chip-to-chip wireless channels, THz communications, channel sounding, channel characterization, channel modeling.**

I. Introduction

Incoming 5G networks promise high speed data transmission for wireless communications. The data rate of 10 Gb/s at 5 GHz frequency band can be achieved with current communication systems based on the new IEEE802.11ax standard, MIMO-OFDM modulation, and complex coding techniques [1]. The IEEE802.11ay standard is expected to offer the peak transmitting data rate of 20 Gb/s at 60 GHz frequency band [2]. The ever-growing capabilities of wireless communication systems that make more data rate available to users fosters the growth of many new applications such as remote surgery, autonomous driving, smart cities, and wireless short range communications. However, for the short range communication between devices in a desktop or on a board, the current wireless communication systems cannot match the required data rate. For example, existing systems use up to 600 Gb/s with InfiniBand HDR 12$\times$ link [3]. Terahertz (THz) frequency band is one of the most promising ways to overcome the gap between wired and wireless communications in computer systems [4] and provide additional communication links between processor and memory or between blades in a data center [5].

The first necessary step to design communication systems for chip-to-chip links inside a desktop is to understand propagation environment inside a metal box and derive statistical characteristics of this channel. At THz frequencies, there has been a large number of measurement campaigns that characterize indoor propagation environment including line-of-sight (LoS) propagation, non-line-of-sight (NLoS) propagation, angles of departure and arrival, shadowing effects, and reflection and diffraction from various materials [5]–[15]. Measurements have also been conducted to characterize waveguide-like structures with different dimensions at 60 and 300 GHz for intra-device communication [16]. Furthermore, on-board THz wireless communication measurements have been conducted by considering different possible scenarios, i.e., LoS, reflected-non-line-of-sight (RNLoS), NLoS and obstructed-line-of-sight (OLoS) [8]. Finally, the channel measurements at 300 GHz inside a desktop size metal enclosure have been performed in [17], [18].

Similarly, several channel models have been proposed for THz wireless channels in indoor environments [19]–[27]. The stochastic channel model based on ray-tracing has been proposed for the propagation channel of THz Kiosk download application in [19]. A scenario-specific stochastic model for THz indoor radio channels has been introduced in [20]. The stochastic model for distance dependent angular and RMS delay spreads has been conducted in [21]. The statistical channel model for THz indoor multipath fading channels has been proposed in [22], [23]. The performances of different large-scale path loss models at 30 GHz, 140 GHz, and 300 GHz have been compared in [24]. The models for characterization of reflections from the surfaces of different materials have been conducted in [25]–[27]. For signal propagation inside a waveguide structure, the channel model based on ray tracing has been proposed in [16].

Compared to the indoor environment, THz propagation in metal enclosures experiences both traveling and resonant waves. This yields to larger number of multiple reflections as well as larger multipath spread [18]. Also, due to the resonant nature of the fields, the received power can vary with transceivers' positions. Based on these findings, a path loss model in an empty desktop size metal enclosure has been presented in [28]. This paper continues this line of work and proposes a general statistical channel model for chip-to-chip communications in metal enclosures. Based on the cavity environment and the statistical properties of the channel inside the metal cavity observed through measurements [18], we first introduce a geometrical model which describes propagation in resonant cavity as a superposition of LoS, single bounced (SB), double bounced (DB), and multi-bounced (MB) rays. Based on the geometrical model, a parametric reference model

This work has been supported, in part, by NSF grant 1651273. The views and findings in this paper are those of the authors and do not necessarily reflect the views of NSF.

has been proposed with the consideration of the signal propagation mechanisms in the excited cavity. Furthermore, a path loss model that captures signal strength variation in resonant cavity is proposed. The frequency correlation functions (FCF) and power delay profiles (PDP) for different possible chip-to-chip communication scenarios are derived from the parametric reference model and compared with the measured ones. The results show a good agreement between the simulated and measured statistics. The first key contribution of the this model is including modeling of resonant modes in the cavity (experimentally discovered in [17]) into statistical channel models, which has not been done before. In contrast to previous statistical channel models that have only single and double bounced rays [23], [25], the proposed model introduces multi-bounced rays with an objective to characterize resonant modes in the cavity. This model characterizes not only the traveling loss, but also the losses due to the resonant modes. The second main contribution of this paper is the new path loss model that considers the losses due to antenna misalignment, which is required for THz wireless communication. Finally, the new model covers large range of real world scenarios, making it very useful modeling tool. Our work focuses on chip-to-chip communications among the components on the motherboard. In particular, we envision wireless broadcasting networks that help with distribution at synchronization messages or short-fast-messaging needed for coherence traffic distribution as discussed in [29], [30]. One example of such a network would be to build a master/slave system by putting antennas and components on the casing of the computer to serve as communication hubs (masters). Communication hubs are used to organize the work and communicate with the on-board devices (slaves) in the area they are responsible for. Our model would be applicable and very useful for the communications between hubs and between hub and devices.

The remainder of the paper is organized as follows. Section II provides a geometrical model that describes propagation mechanisms inside a metal cavity. Based on the geometrical model, Section III proposes the parametric reference model. Section IV proposes the path loss model that captures signal fluctuation due to resonant waves. Section V derives the correlation function from the proposed parametric reference model. Section VI verifies the path loss and statistical channel model by comparing the simulated path loss and PDPs with measured results for different possible scenarios. Section VII provides concluding remarks.

II. Geometrical Model

This section introduces a geometrical model that characterizes THz chip-to-chip channel inside a desktop size metal enclosure. In [18], we have found that both traveling waves and resonant modes exist inside the metal cavity. To capture these propagation mechanisms, we first introduce an integrated geometrical model which describes propagation in resonant cavity as a superposition of LoS, single bounced (SB), double bounced (DB), and multi-bounced (MB) rays.

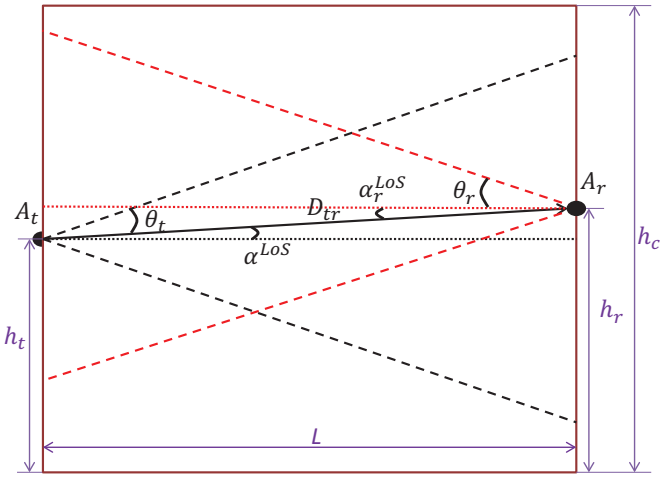

Fig. 1. The geometrical model for LoS propagation link.

A. Geometrical Model for LoS Rays

Figure 1 shows the geometrical model for the LoS propagation inside a desktop size metal cavity whose length and height are denoted by L and h_c. As shown in Fig. 1, the antennas of Tx and Rx are denoted by A_t and A_r, respectively, which are assumed to be located on the opposite sidewalls of the metal cavity. The height and half-beamwdith of A_t are represented by h_t and θ_t, and for A_r by h_r, and θ_r, respectively. The angles α_t^{LoS} and α_r^{LoS} denote the departure and arrival angles of the LoS propagating signal, respectively. The angles α_t^{LoS} and α_r^{LoS} are limited by the beamwidths of A_t and A_r, which means that $-\theta_t \leq \alpha_t^{LoS} \leq \theta_t$ and $-\theta_r \leq \alpha_r^{LoS} \leq \theta_r$. With the introduction of α_t^{LoS} and α_r^{LoS}, the model could handle the loss due to vertical misalignment between the Tx and the Rx. This is very common for the LoS links in on-board chip-to-chip communication, e.g. the CPU (Central Processing Unit) to AGP (Accelerated Graphics Port) link. The distance between A_t and A_r is denoted by D_{tr}, which also represents the signal traveling distance for the LoS scenario.

B. Geometrical Model for Single Bounced Rays

Figure 2 shows single-reflected rays inside the metal cavity. It is assumed that there are M scatters seen by the Tx inside the cavity. These M scatters are clustered into J groups based on the distances from the Tx. For each group, scatters are aligned vertically on a line that is parallel to the sidewalls of the cavity on which the transceivers are located. As shown in Fig. 2, the distance from the Tx to the j^{th} group of the scatters seen by the Tx is denoted by R_t^j, where $1 \leq j \leq J$. The symbols R_{t1} and R_{t2} denote the lower and upper bounds of R_t^j for which $0 \leq R_{t1} \leq R_t^j \leq R_{t2} \leq L$. The j^{th} group contains $M^{(j)}$ scatters hence $\sum_{j=1}^{J} M^{(j)} = M$. The m^{th} scatter from the j^{th} group of the scatters is represented by $S^{(j,m)}$, where $1 \leq m \leq M^{(j)}$. For the single-bounced reflections, it is assumed that the signal from the Tx travels to the Rx by reflecting from only one of the scatters seen by the Tx, i.e. $S^{(j,m)}$. The distance traveled by the SB ray is calculated as $\epsilon_t^{(j,m)} + \epsilon_r^{(j,m)}$, where $\epsilon_t^{(j,m)}$ and $\epsilon_r^{(j,m)}$ represent

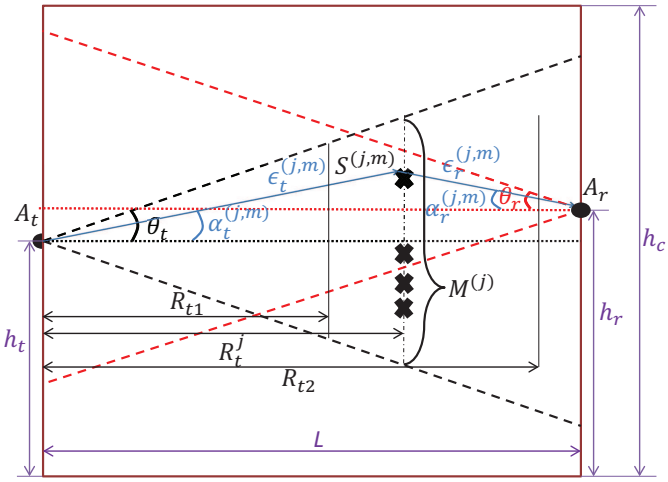

Fig. 2. The geometrical model for single bounced rays.

the distance from A_t to $S^{(j,m)}$ and the distance from $S^{(j,m)}$ to A_r, respectively. The angles $\alpha_t^{(j,m)}$ and $\alpha_r^{(j,m)}$ denote the angles of departure and the angles of arrival, respectively. The departure and arrival angles are limited by the beamwidths of A_t and A_r, respectively.

C. Geometrical Model for Double Bounced Rays

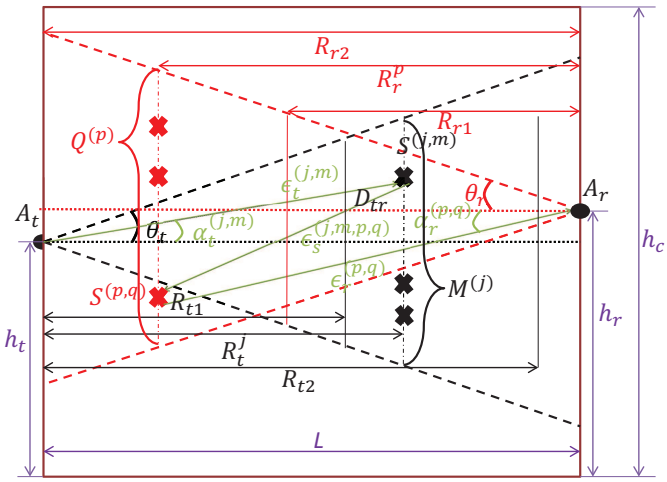

Fig. 3. The geometrical model for double bounced rays.

For double bounced rays, in addition to the M scatters defined in section II-B, it is assumed that there are additional Q scatters seen by the Rx as shown in Fig. 3. Similarly, these Q scatters are categorized into P groups according to the distances from the Rx. The R_r^p denotes the distance between the p^{th} group of scatters and Rx, where $1 \leq p \leq P$. Also, R_r^p is bounded by R_{r1} and R_{r2} for which $0 \leq R_{r1} \leq R_r^p \leq R_{r2} \leq L$. There are $Q^{(p)}$ scatters in total in the p^{th} group of scatters and $\sum_{p=1}^{P} Q^{(p)} = Q$. Scatter $S^{(p,q)}$ represents the q^{th} scatter at the p^{th} group of scatters, where $1 \leq q \leq Q^{(p)}$. For the DB rays, the signal from the Tx randomly hits one scatter seen by the Tx, then bounces to another scatter seen by the Rx, and finally travels to the Rx, i.e. $A_t \rightarrow S^{(j,m)} \rightarrow S^{(p,q)} \rightarrow A_r$ as shown in Fig. 3. The traveling distances of $A_t \rightarrow S^{(j,m)}$, $S^{(j,m)} \rightarrow S^{(p,q)}$, and $S^{(p,q)} \rightarrow A_r$ are denoted as $\epsilon_t^{(j,m)}$, $\epsilon_s^{(j,m,p,q)}$, and $\epsilon_r^{(p,q)}$. The departure angle $\alpha_t^{(j,m)}$ is defined in the Section II-B, the angle $\alpha_r^{(p,q)}$ is defined as the arrival angle of the ray which reflects from the scatter $S^{(p,q)}$.

D. The Geometrical Model for Multi-Bounced Rays

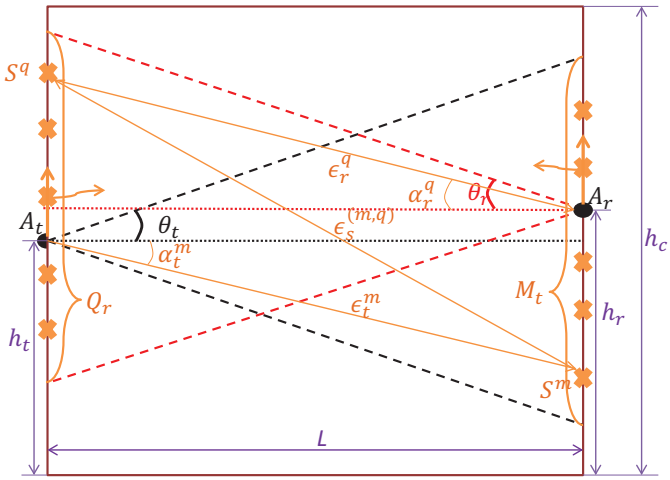

Fig. 4. The geometrical model for multi-bounced rays.

Unlike the propagation in free space environment, the traveling wave inside the metal enclosure is likely to excite the cavity, which means that the transceiver sidewalls of the cavity can be treated both as consecutive scatters and the sources of EM waves. The propagation of the generated EM waves, again, can be characterized as LoS, SB, and DB rays. To simplify the modeling, only LoS propagation of the generated EM waves are considered and modeled as multi-bounced (MB) rays for which the signals periodically bounce back and forth between the transceiver sidewalls of the metal cavity. As shown in Fig. 4, it is assumed that the Rx sidewall consists of M_t scatters seen by the Tx, and the Tx sidewall consists of Q_r scatters seen by the Rx. The m^{th} scatter on the Rx sidewall is denoted as S^m, where $1 \leq m \leq M_t$. Similarly, S^q represents the q^{th} scatter on the Tx sidewall, where $1 \leq q \leq Q_r$. The distance of $A_t \rightarrow S^m$, $S^m \rightarrow S^q$, and $S^q \rightarrow A_r$ are denoted as ϵ_t^m, $\epsilon_s^{(m,q)}$, and ϵ_r^q, respectively. The angle α_t^m represents the angle of departure for the ray that hits the scatter S^m, and the angle α_r^q represents the angle of arrival for the ray that reflects from the scatter S^q. Both α_t^m and α_r^q are limited by the beamwidths of A_t and A_r.

E. Integrated Geometrical Model

The integrated geometrical model is shown in Fig. 5. It includes all possible reflection conditions described previously, i.e. LoS, SB, DB, and MB. All parameters defined in the geometrical model are summarized in Table I. It is observed that the distances D_{tr}, $\epsilon_t^{(j,m)}$, $\epsilon_r^{(j,m)}$, $\epsilon_s^{(j,m,p,q)}$, $\epsilon_r^{(p,q)}$, ϵ_t^m, $\epsilon_s^{(m,q)}$, ϵ_r^q, and angles α_t^{LoS}, α_r^{LoS}, $\alpha_r^{(j,m)}$ can be either directly

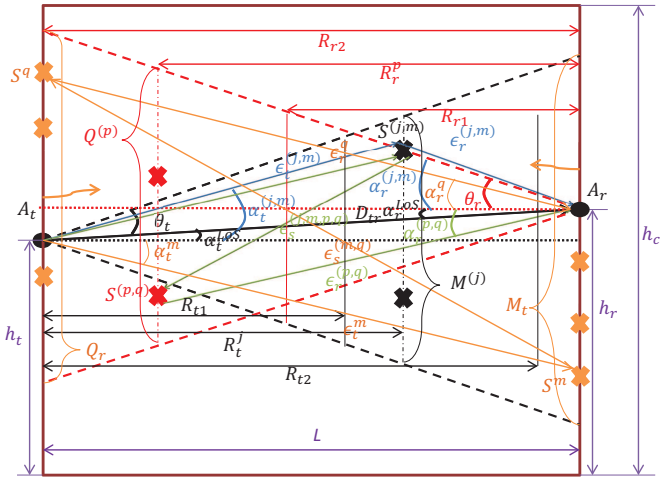

Fig. 5. The intact geometrical model for chip-to-chip wireless communication channel in a desktop size metal cavity.

obtained from the plots or expressed as functions of the random variables $\alpha_t^{(j,m)}$, $\alpha_r^{(p,q)}$, R_t^j, and R_r^p as follows:

$$D_{tr} = \sqrt{L^2 + (h_t - h_r)^2}, \tag{1}$$

$$\epsilon_t^{(j,m)} = \frac{R_t^j}{\cos\left(\alpha_t^{(j,m)}\right)}, \tag{2}$$

$$\epsilon_r^{(j,m)} = \sqrt{\left(L - R_t^j\right)^2 + \left(R_t^j \tan\left(\alpha_t^{(j,m)}\right) + h_t - h_c\right)^2}, \tag{3}$$

$$\epsilon_s^{(j,m,p,q)} = \left[\left(R_t^j + R_r^p - L\right)^2 + \left(R_t^j \tan\left(\alpha_t^{(j,m)}\right) - R_r^p \tan\left(\alpha_r^{(p,q)}\right) + h_t - h_r\right)^2\right]^{\frac{1}{2}}, \tag{4}$$

$$\epsilon_r^{(p,q)} = \frac{R_r^p}{\cos\left(\alpha_r^{(p,q)}\right)}, \tag{5}$$

$$\epsilon_t^m = \frac{L}{\alpha_t^m}, \tag{6}$$

$$\epsilon_s^{(m,q)} = \sqrt{\left(L\tan\left(\alpha_t^m\right) - L\tan\left(\alpha_r^q\right) + h_t - h_r\right)^2 + L^2}, \tag{7}$$

$$\epsilon_r^q = \frac{L}{\alpha_r^q}, \tag{8}$$

$$\alpha_t^{LoS} = arctan(\frac{h_r - h_t}{L}), \tag{9}$$

$$\alpha_r^{LoS} = arctan(\frac{h_t - h_r}{L}), \tag{10}$$

$$\alpha_r^{(j,m)} = \arctan(\frac{R_t^j \tan(\alpha_t^{(j,m)}) + h_t - h_r}{L - R_t^j}). \tag{11}$$

The derivations of more complex expressions such as those in (3), (4), (7), and (11) are shown in Appendix A. Other derivations are omitted for brevity.

III. Reference Model

From the geometrical model, the time-invariant input delay-spread function of the Tx - Rx link can be expressed as the superposition of the LoS, SB, DB, and MB rays as

$$h(t,\tau) = h_{LoS}(t,\tau) + h_{SB}(t,\tau) + h_{DB}(t,\tau) + h_{MB}(t,\tau). \tag{12}$$

Since the chip-to-chip wireless channel being discussed in this paper is stationary with a fixed h_t and h_r, the parameter t will be omitted in further discussions.

The LoS component of the input delay-spread function can be expressed as

$$h_{LoS}(\tau) = \sqrt{\frac{K}{K+1}} A_{LoS} e^{j\phi_{LoS}} \delta(\tau - \tau_{LoS}), \tag{13}$$

where K is the Ricean factor; ϕ_{LoS} represents the LoS phase delay; $\tau_{LoS} = \frac{D_{tr}}{c_0}$ is the LoS time delay and c_0 is the speed of light; A_{LoS} represents the LoS amplitude and can be expressed as $A_{LoS} = \sqrt{P_t G_t G_r / PL_{LoS}}$, where P_t, G_t, G_r, and PL_{LoS} represent transmit power, the Tx antenna gain, the Rx antenna gain, and the LoS path loss, respectively.

The single-bounced component, $h_{SB}(\tau)$, of the input delay-

TABLE I
Definitions of Parameters Introduced in the Statistical Geometrical Model.

h_c	Height of the cavity
L	Length of the cavity
h_t, h_r	Height of the Tx and Rx
A_t, A_r	The Tx and Rx antennas
θ_t, θ_r	Half-beamwidth of the Tx and Rx antennas
$\alpha_t^{LoS}, \alpha_r^{LoS}$	Departure and arrival angles of LoS propagating signal
D_{tr}	The distance between the Tx and Rx
M	The number of scatters seen by the Tx
J	The number of groups the M scatters are categorized
R_t^j	The distance between the Tx and the j^{th} group of scatters seen by the Tx
R_{t1}, R_{t2}	The minimum and maximum bounds of R_t^j
$M^{(j)}$	The number of scatters contained in the j^{th} group
$S^{(j,m)}$	The m^{th} scatter at the j^{th} group of scatters seen by the Tx
$\epsilon_t^{(j,m)}$	The distance between A_t and $S^{(j,m)}$
$\epsilon_r^{(j,m)}$	The distance between $S^{(j,m)}$ and A_r
$\alpha_t^{(j,m)}$	The departure angle of the ray that hits $S^{(j,m)}$
$\alpha_r^{(j,m)}$	The arrival angle of the ray that reflects from $S^{(j,m)}$
Q	The number of scatters seen by the Rx
P	The number of groups the Q scatters are categorized
R_r^p	The distance between the Rx and the p^{th} group of scatters seen by the Rx
R_{r1}, R_{r2}	The minimum and maximum bounds of R_r^p
$Q^{(p)}$	The number of scatters contained in the p^{th} group
$S^{(p,q)}$	The q^{th} scatter at the p^{th} group of scatters seen by the Rx
$\epsilon_s^{(j,m,p,q)}$	The distance between $S^{(j,m)}$ and $S^{(p,q)}$
$\epsilon_r^{(p,q)}$	The distance between $S^{(p,q)}$ and A_r
$\alpha_r^{(p,q)}$	The arrival angle of the ray that reflects from $S^{(p,q)}$
M_t, Q_r	The number of scatters constitute the Rx and Tx sidewalls
S^m, S^q	The m^{th} and q^{th} scatters on the Rx and Tx sidewall
α_t^m	The departure angle of the ray that hits S^m
α_r^q	The arrival angle of the ray that reflects from S^q
ϵ_t^m	The distance between A_t and S^m
$\epsilon_s^{(m,q)}$	The distance between S^m and S^q
ϵ_r^q	The distance between S^q and A_r

spread can be written as

$$h_{SB} = \sqrt{\frac{\eta_{SB}}{K+1}} \lim_{M\to\infty} \frac{1}{\sqrt{M}} \sum_{j=1}^{J} \sum_{m=1}^{M^{(j)}} A_{SB}^{(j,m)} e^{j\phi_{SB}^{(j,m)}} \delta(\tau - \tau_{SB}^{(j,m)}), \quad (14)$$

where η_{SB} represents the relative power allocated to the SB rays; $A_{SB}^{j,m}$, $\phi_{SB}^{(j,m)}$, and $\tau_{SB}^{(j,m)}$ represent the amplitude, phase, and time delay of multipath components, respectively. The amplitude of the multipath component can be written as $A_{SB}^{(j,m)} = \sqrt{P_t G_t G_r / PL_{SB}^{(j,m)}}$, where $PL_{SB}^{(j,m)}$ represents the path loss of the single bounced component. The time delay $\tau_{SB}^{(j,m)}$ is equal to $\left(\epsilon_t^{(j,m)} + \epsilon_r^{(j,m)}\right)/c_0$.

The double-bounced component, h_{DB} can be expressed as

$$h_{DB}(\tau) = \sqrt{\frac{\eta_{DB}}{K+1}} \frac{1}{\sqrt{MQ}} \sum_{j,m=1}^{J,M^{(j)}} \sum_{p,q=1}^{P,Q^{(p)}} A_{DB}^{(j,m,p,q)} e^{j\phi_{DB}^{(j,m,p,q)}} \delta(\tau - \tau_{DB}^{(j,m,p,q)}), \quad (15)$$

where η_{DB} is the relative power allocated to the DB rays; $A_{DB}^{(j,m,p,q)}$, $\phi_{DB}^{(j,m,p,q)}$, and $\tau_{DB}^{(j,m,p,q)}$ represent the amplitude, phase, and time delay of the multipath components, respectively. Similarly, the amplitude can be written as $A_{DB}^{(j,m,p,q)} = \sqrt{P_t G_t G_r / PL_{DB}^{(j,m,p,q)}}$, where $PL_{DB}^{(j,m,p,q)}$ is the path loss of DB component. Same as the expressions in the SB condition, the time delay can be calculated as $\left(\epsilon_t^{(j,m)} + \epsilon_s^{(j,m,p,q)} + \epsilon_r^{(p,q)}\right)/c_0$.

The MB component can be written as

$$h_{MB}(\tau) = \sqrt{\frac{\eta_{MB}}{K+1}} \lim_{M_t,Q_r} \frac{1}{\sqrt{M_t Q_r}} \sum_{n=1}^{N} \sum_{m=1}^{M_t} \sum_{q=1}^{Q_r} \sqrt{k_n} A_{MB}^{(n,m,q)} e^{j\phi_{MB}^{(n,m,q)}} \delta(\tau - \tau_{MB}^{(n,m,q)}), \quad (16)$$

where η_{MB} is the relative power allocated to the MB rays. The sum of η_{SB}, η_{DB}, and η_{MB} is unity. Here, N is the number of later arriving rays and k_n represents the relative power contributed by the n^{th} later arriving ray and it follows that $\sum_{n=1}^{N} k_n = 1$. The parameter A_{MB} represents the amplitude of the multi-bounced component and can be calculated as $A_{MB}^{(n,m,q)} = \sqrt{P_t G_t G_r / PL_{MB}^{(n,m,q)}}$, where $PL_{MB}^{(n,m,q)}$ represents the corresponding path loss. The expressions of PL_{LoS}, $PL_{SB}^{(j,m)}$, $PL_{DB}^{(j,m,p,q)}$, and $PL_{MB}^{(n,m,q)}$ are derived in section IV. The Parameter $\phi_{MB}^{(n,m,q)}$ represents the phase delay of MB rays. It is assumed that ϕ_{LoS}, $\phi_{SB}^{(j,m)}$, $\phi_{DB}^{(j,m,p,q)}$, and $\phi_{MB}^{(n,m,q)}$ are uniform random variables on the interval $[-\pi, \pi)$ and are independent from the angles of departure and the angles of arrival. The Parameter $\tau_{MB}^{(n,m,q)}$ represents the time delay of the multipath component. It can be calculated same as the corresponding parameters in the SB and DB conditions with the signal traveling distance of $\epsilon_t^m + \epsilon_r^q + (2n-1)\epsilon_{avg}$, where $2n-1$ represents the number of times that the signal bounces back and forth between the transceiver sidewalls and ϵ_{avg} represents the average of the distances between the scatters on the Rx sidewall and the scatters on the Tx sidewall and can be calculated as

$$\epsilon_{avg} = \frac{1}{M_t Q_r} \sum_{m=1}^{M_t} \sum_{q=1}^{Q_r} \epsilon_s^{(m,q)}. \quad (17)$$

To simplify further analysis, we use the time-invariant transfer function which is the Fourier transform of the input delay-spread function and can be written as [31]

$$T(f) = \mathcal{F}_\tau\{h(\tau)\} = T_{LoS}(f) + T_{SB}(f) + T_{DB}(f) + T_{MB}(f), \quad (18)$$

where $T_{LoS}(f)$, $T_{SB}(f)$, $T_{DB}(f)$, and $T_{MB}(f)$ are LoS, SB, DB, and MB components of the transfer function and can be written, respectively, as

$$T_{LoS}(f) = \sqrt{\frac{K}{k+1}} A_{LoS} e^{j\phi_{LoS} - j2\pi f \tau_{LoS}}, \quad (19)$$

$$T_{SB}(f) = \sqrt{\frac{\eta_{SB}}{K+1}} \lim_{M\to\infty} \frac{1}{\sqrt{M}} \sum_{j=1}^{J} \sum_{m=1}^{M^{(j)}} A_{SB}^{(j,m)} e^{j\phi_{SB}^{(j,m)} - j2\pi f \tau_{SB}^{(j,m)}}, \quad (20)$$

$$T_{DB}(f) = \sqrt{\frac{\eta_{DB}}{K+1}} \frac{1}{\sqrt{MQ}} \sum_{j,m=1}^{J,M^{(j)}} \sum_{p,q=1}^{P,Q^{(p)}} A_{DB}^{(j,m,p,q)} e^{j\phi_{DB}^{(j,m,p,q)} - j2\pi f \tau_{DB}^{(j,m,p,q)}}, \quad (21)$$

$$T_{MB}(f) = \sqrt{\frac{\eta_{MB}}{K+1}} \lim_{M_t,Q_r} \frac{1}{\sqrt{M_t Q_r}} \sum_{n=1}^{N} \sum_{m=1}^{M_t} \sum_{q=1}^{Q_r} \sqrt{k_n} A_{MB}^{(n,m,q)} e^{j\phi_{MB}^{(n,m,q)} - j2\pi f \tau_{MB}^{(n,m,q)}}. \quad (22)$$

IV. Path Loss Model

The THz wireless channel inside a metal enclosure is much more complex than the statistical communication channel in free space because of the cavity effect introduced by the metal enclosure. For this channel, the Friis equation is not sufficient to provide an approximate path loss prediction. Therefore, a new path loss model is derived to describe path loss in this channel. From the channel characterization, it is found that both traveling wave and resonant modes exist inside the box [18]. Therefore, another term is required to describe the effect of the resonant modes. Additionally, to compensate the high path loss of THz channel, both Tx and Rx are used with high gain antennas. Hence, the radiation pattern of the antennas should also be considered. In addition, molecular absorption at THz frequencies can be significant, but the calculated results based on the equation in [32] and the measured values in [33] show that it is negligible at the distance less than 1 m. For our measurement setup, the maximum distance is 30.5 cm and the loss due to molecular absorption is about 0.066 dB, which can be neglected.

For the THz wireless channel in metal enclosure, the theoretical path loss $(PL)_{dB}$ can be calculated as

$$(PL)_{dB} = \overline{(PL)^t}_{dB} + 10log_{10}(|E|^2)^{-1} + 10log_{10}([g(\alpha_t)g(\alpha_r)]^2)^{-1} + X_\sigma, \quad (23)$$

where $\overline{(PL)^t}$ is the mean path loss of traveling wave and can be calculated by averaging Friis formula over the frequency band as

$$\overline{(PL)^t} = \frac{1}{\Delta f}\int_{\Delta f}\left(\frac{4\pi D^{\frac{\gamma}{2}} f}{c_0}\right)^2 df, \tag{24}$$

where D represents the signal traveled distance, γ is the path loss exponent, and c_0 is the speed of light.

The parameter $10\log_{10}(|E|^2)^{-1}$ which depends on h_r, represents the received power variation contributed by resonating modes and is defined as in [28].

The parameter $10log_{10}([g(\alpha_t)g(\alpha_r)]^2)^{-1}$ describes the loss due to the misalignment of the Tx and Rx. The angles α_t and α_r which are functions of h_t and h_r represent the departure and arrival angles, respectively. The parameter $g(\alpha)$ is the radiation pattern of the antenna. Here, diagonal horn antenna has been used for measurements for which $g(\alpha)$ can be written as [34]

$$g(\alpha) = \begin{cases} X + Ycos(Z\alpha) & -\theta \le \alpha \le \theta \\ c & otherwise \end{cases}, \tag{25}$$

where $-\theta$ and θ define the beamwidth of the Tx and Rx antennas and c is a small constant.

X_σ is a zero-mean Gaussian random variable with standard deviation σ. It describes the random shadowing effects. To simplify the modeling, X_σ will be set to zero in further discussions. The path loss model which is determined by h_t and h_r describes the channel fading with respect to the vertical positioning of transceivers.

Path loss for LoS, SB, DB, and MB rays can be calculated using (23) and (24). For LoS propagation, by taking the signal traveled distance $D = D_{tr}$, departure angles $\alpha_t = \alpha_t^{LoS}$, and arrival angles $\alpha_r = \alpha_r^{LoS}$, PL_{LoS} can be calculated as

$$(PL_{LoS})_{dB} = 10log_{10}\left(\frac{1}{\Delta f}\int_{\Delta f}\left(\frac{4\pi D_{tr}^{\frac{\gamma}{2}} f}{c_0}\right)^2 df\right) + 10log_{10}(|E|^2)^{-1} + 10log_{10}([g(\alpha_t^{LoS})g(\alpha_r^{LoS})]^2)^{-1} + X_\sigma. \tag{26}$$

Similarly, the path loss for single bounced rays ($PL_{SB}^{(j,m)}$), double bounced rays ($PL_{DB}^{(j,m,p,q)}$), and multi-bounced rays ($PL_{MB}^{(n,m,q)}$) can be calculated as

$$(PL_{SB}^{(j,m)})_{dB} = \overline{(PL_{SB}^{(j,m)})^t}_{dB} + 10log_{10}(|E|^2)^{-1} + 10log_{10}([g(\alpha_t^{(j,m)})g(\alpha_r^{(j,m)})]^2)^{-1}, \tag{27}$$

$$(PL_{DB}^{(j,m,p,q)})_{dB} = \overline{(PL_{DB}^{(j,m,p,q)})^t}_{dB} + 10log_{10}(|E|^2)^{-1} + 10log_{10}([g(\alpha_t^{(j,m)})g(\alpha_r^{(p,q)})]^2)^{-1}, \tag{28}$$

$$(PL_{MB}^{(n,m,q)})_{dB} = \overline{(PL_{MB}^{(n,m,q)})^t}_{dB} + 10log_{10}(|E|^2)^{-1} + 10log_{10}([g(\alpha_t^{m})g(\alpha_r^{q})]^2)^{-1}, \tag{29}$$

where $\overline{(PL_{SB}^{(j,m)})^t}$, $\overline{(PL_{DB}^{(j,m,p,q)})^t}$, and $\overline{(PL_{MB}^{(n,m,q)})^t}$ can be written as

$$\overline{(PL_{SB}^{(j,m)})^t} = \frac{1}{\Delta f}\int_{\Delta f}\left(\frac{4\pi\left(\epsilon_t^{(j,m)} + \epsilon_r^{(j,m)}\right)^{\frac{\gamma}{2}} f}{c_0}\right)^2 df, \tag{30}$$

$$\overline{(PL_{DB}^{(j,m,p,q)})^t} = \frac{1}{\Delta f}\int_{\Delta f}\left(\frac{4\pi\left(\epsilon_t^{(j,m)} + \epsilon_s^{(j,m,p,q)} + \epsilon_r^{(p,q)}\right)^{\frac{\gamma}{2}} f}{c_0}\right)^2 df, \tag{31}$$

$$\overline{(PL_{MB}^{(n,m,q)})^t} = \frac{1}{\Delta f}\int_{\Delta f}\left(\frac{4\pi\left(\epsilon_t^{m} + \epsilon_{avg} + \epsilon_r^{q}\right)^{\frac{\gamma}{2}} f}{c_0}\right)^2 df. \tag{32}$$

V. Correlation Function of Wireless Channel for Chip-to-chip Communication in Metal Enclosure

Auto-correlation function is the correlation of a signal and its delayed copy as a function of the delay. It is a mathematical tool for finding the repeat patterns. The normalized auto-correlation function of the transfer function defined in (18) is defined as

$$R(\Delta f) = \frac{E[T(f)^* T(f+\Delta f)]}{\sqrt{Var[T(f)]Var[T(f)]}}, \tag{33}$$

where $(\cdot)^*$ represents the complex conjugate operation, $\mathrm{E}[\cdot]$ denotes the statistical expectation operator, and $\mathrm{Var}[\cdot]$ is the statistical variance operator.

Since $T_{SB}(f)$, $T_{DB}(f)$, and $T_{MB}(f)$ are independent complex Gaussian random processes, (33) can be simplified to

$$R(\Delta f) = R_{LoS}(\Delta f) + R_{SB}(\Delta f) + R_{DB}(\Delta f) + R_{MB}(\Delta f), \tag{34}$$

where $R_{LoS}(\Delta f)$, $R_{SB}(\Delta f)$, $R_{DB}(\Delta f)$, and $R_{MB}(\Delta f)$ are auto-correlation functions of LoS, single-bounced, double-bounced, and multi-bounced components, respectively, and can be written as

$$R_{LoS}(\Delta f) = \frac{E[T_{LoS}(f)^* T_{LoS}(f+\Delta f)]}{\Omega}, \tag{35}$$

$$R_{SB}(\Delta f) = \frac{E[T_{SB}(f)^* T_{SB}(f+\Delta f)]}{\Omega}, \tag{36}$$

$$R_{DB}(\Delta f) = \frac{E[T_{DB}(f)^* T_{DB}(f+\Delta f)]}{\Omega}, \tag{37}$$

$$R_{MB}(\Delta f) = \frac{E[T_{MB}(f)^* T_{MB}(f+\Delta f)]}{\Omega}, \tag{38}$$

where $\Omega = P_t G_t G_r / PL_{LoS}$.

Since the number of scatters defined in the reference model is close to infinity, the departure angles ($\alpha_t^{(j,m)}$ and α_t^m), the arrival angles ($\alpha_r^{(p,q)}$ and α_r^q), the distances between the j^{th} group of scatters and the Tx (R_t^j), and the distance between the p^{th} group of scatters and the Rx (R_r^p), which are defined in the geometrical model, can be replaced with the independent uniform distributed continuous random variables

α_t, α_r, R_t, and R_r whose probability density functions (pdf) $f(\alpha_t)$, $f(\alpha_r)$, $f(R_t)$, and $f(R_r)$ can be written, respectively, as

$$f(\alpha_t) = \frac{1}{2\theta_t}, \tag{39}$$

$$f(\alpha_r) = \frac{1}{2\theta_r}, \tag{40}$$

$$f(R_t) = \frac{1}{R_{t2} - R_{t1}}, \tag{41}$$

$$f(R_r) = \frac{1}{R_{r2} - R_{r1}}. \tag{42}$$

By taking (19) into (35), (20) into (36), (21) into (37), and (22) into (38), the auto-correlation functions of the LoS, SB, DB, and MB components can be calculated, respectively, as

$$R_{LoS} = \frac{K}{K+1} e^{\frac{-j2\pi\Delta f D_{tr}}{c_0}}, \tag{43}$$

$$R_{SB} = \frac{\eta_{DB}}{K+1} \int_{R_{t1}}^{R_{t2}} \int_{-\theta_t}^{\theta_t} \frac{PL_{LoS}}{PL_{SB}} e^{-j2\pi\Delta f \tau_{SB}} f(R_t) f(\alpha_t) d\alpha_t dR_t, \tag{44}$$

$$R_{DB} = \frac{\eta_{DB}}{K+1} \int_{R_{t1}}^{R_{t2}} \int_{R_{r1}}^{R_{r2}} \int_{-\theta_t}^{\theta_t} \int_{-\theta_r}^{\theta_r} \frac{PL_{LoS}}{PL_{DB}} e^{-j2\pi\Delta f \tau_{DB}} f(R_t) f(R_r) f(\alpha_t) f(\alpha_r) d\alpha_r d\alpha_t dR_r dR_t, \tag{45}$$

$$R_{MB} = \frac{\eta_{MB}}{K+1} \sum_{n=1}^{N} k_n \int_{-\theta_t}^{\theta_t} \int_{-\theta_r}^{\theta_r} \frac{PL_{LoS}}{PL_{MB}} e^{-j2\pi\Delta f \tau_{MB}} d\alpha_r d\alpha_t. \tag{46}$$

The calculation and full expression of the auto-correlation functions for SB, DB, and MB components are derived in the Appendix B. Please note that these auto-correlation functions must be evaluated numerically since the integrals in (44), (45), and (46) do not have closed-form solutions.

VI. Model Verification

In this section, we compare the simulation and measurement results for path loss and PDP to verify the proposed model. Path loss represents the power attenuation as the signal propagates through space, and PDP provides the intensity of a signal received through a multipath channel as a function of time delay. Also, some other important parameters such as mean excess delay, RMS delay spread, and coherence bandwidth are calculated from the PDP. The path loss model is provided in (23) as a function of h_t and h_r. The PDP of the proposed model can be calculated by taking the Inverse Fourier Transform of the auto-correlation function of the wireless channel in the metal cavity, i.e.,

$$p(\tau) = \mathcal{F}_{\Delta f}^{-1}\{R(\Delta f)\}. \tag{47}$$

Since any change inside the cavity can influence the propagation of the signal in the metal cavity, a set of measurements were performed in a desktop size, 30.5 cm$\times$ 30.5 cm$\times$ 9.6 cm, metal enclosure with different possible scenarios being considered.

The first scenario is the LoS propagation without any obstructions in between, which is equivalent to empty metal cavity. Measurements were performed in the desktop size empty metal cavity by varying the transceivers' heights h_t and h_r together from 0 cm to 6.6 cm with the step size of 0.6 cm. Figure 6a shows the measurement setup. A description of this measurement can be found in [17]. The antennas being used in this measurement are diagonal horn antennas whose gain varies between 22 dBi and 23 dBi with the 3 dB beamwidths about 12°, i.e., $2\theta_t = 2\theta_r = 12°$. We curve-fit the EM simulated radiation pattern (obtained by using CST v17) of the diagonal horn antenna. The parameters of the radiation pattern $g(\alpha)$ are $X = 0.54$, $Y = 0.45$, $Z = 11.15$, and $c = 0.01$. The measured data was collected at the frequency of 300 GHz with bandwidth of 12 GHz.

Figure 6b compares the calculated path loss using (23) with the measured results. It can be seen from the plot that the theoretical and measured mean path loss match very well. The resonant modes defined in (23) and their corresponding coefficients can be found using curve-fitting as shown in [17]. For each height, we performed three measurements and the variation between different measured results is very small. This is because the channel is stationary with fixed h_r and h_t, which means that there are no temporal or spatial variations in the channel which would lead to significant change of the path loss. Although some shadowing can still be observed, this may be due to the variation of the resonant modes inside the cavity. Please note that this shadowing may not be a traditional shadowing effect and is just a random process which leads to a small variation in the received power with fixed h_t and h_r. The path loss model parameters γ and σ are estimated to be 1.9874 and 0.01682 dB via least square linear fitting through measured scatter points.

Figure 6c shows the simulated and measured normalized correlation functions. As seen from the plot, the correlation functions for the simulation and measurement match with each other and oscillate around 0.97. This is because they include both traveling wave and resonance due to the cavity effect.

Figure 6d compares the simulated and measured PDP for the case $h_t = h_r = 2.4$ cm. Measured PDP shows that there are several clusters of peaks that arrive with delay of 2.05 ns after the first arriving peak. This delay indicates that between any two adjacent clusters of peaks, the extra distance covered by the later arriving signal is 61.5 cm which is twice of the cavity's length. This implies that these periodic later arriving peaks are the consequences of the EM fields generated from the excited sidewalls (sidewalls A and C as shown in Fig. 6a) of the cavity. To simplify the analysis, these periodic later arriving peaks are treated as the results of multiple bounces of the traveling wave between the walls of the cavity where Tx and Rx are positioned. In the reference model, the Ricean factor K is estimated to be 1.55. Since measurement was performed without any scatters between the Tx - Rx link, there are no single-bounced and double-bounced rays. Therefore, parameters η_{SB} and η_{DB} are set to 0 and η_{MB} is set to 1. For the MB component, the number of later arriving rays

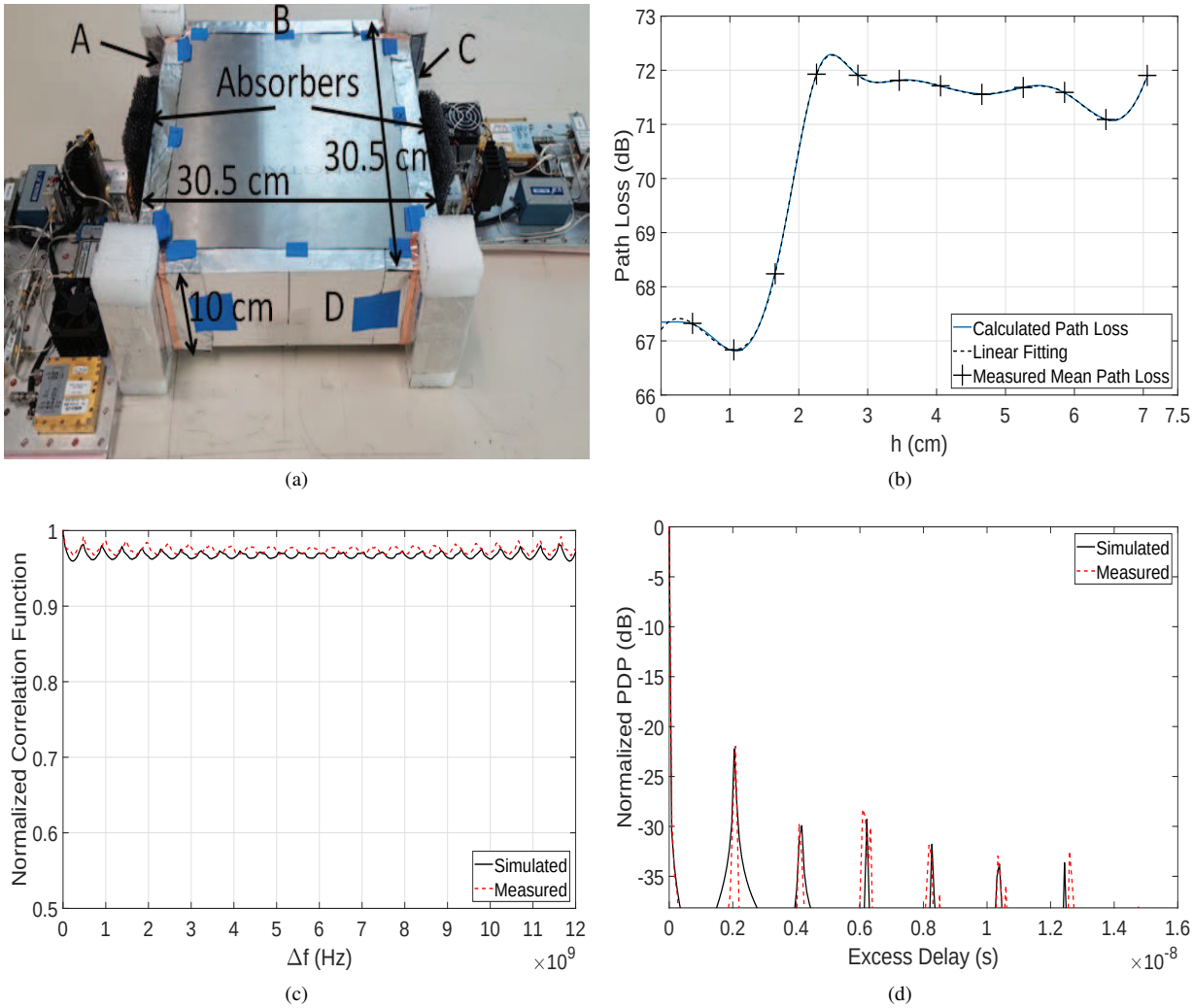

Fig. 6. LoS propagation in an empty metal cavity at 300 GHz with h_t and h_r varying together from 0 cm to 6.6 cm: (a) Measurements setup, (b) Comparison of the theoretical and measured path loss with respect to h, (c) Comparison of the normalized correlation functions, and (d) Comparison of the normalized simulated and measured PDPs.

is selected to be 6. Parameters $k_1 = k_3 = k_4 = 0.1667$, $k_2 = 0.1$, and $k_5 = k_6 = 0.2$. It can be found from (43) and (62) that $R_{LoS}(\Delta f)$ and $R_{MB}(\Delta f)$ are independent with respect to R_t and R_r. Therefore, in this case, the values of R_{t1}, R_{t2}, R_{r1}, and R_{r2} do not affect the results of the simulations. It can be observed from Fig. 6b that the simulated PDP matches well with the measured PDP in amplitudes and excess delays. The mismatch towards larger excess delay is due to the noise floor which was not accounted for in the theoretical model.

Another potential scenario is the LoS propagation with a misalignment of the Tx and Rx. As shown in Fig. 7a, a set of measurements have been performed with h_t being fixed at 2.4 cm and h_r being varied from 0 cm to 6.6 cm with the step size of 0.6 cm to prove the proposed path loss model. The measured data of one case with $h_t = 2.4$ cm and $h_r = 4.8$ cm is selected from these measurements to verify the proposed channel model by comparing the simulated and measured PDP values.

Figure 7b compares the calculated and measured path loss. From the plot, a good agreement can be observed, which illustrates the effectiveness of the proposed path loss model. From the measurements, the parameters γ and σ defined in equation (23) are estimated to be 1.98 and 0.02259 dB. Table II compares the proposed path loss model (PM) parameters for the scenarios discussed in the paper and the parameters of the floating-intercept model (FI) for indoor communication scenario at 300 GHz [24]. Please note that in contrast to the FI model which measures the path loss with respect to the distance between the transceivers, the proposed model predicts the path loss with respect to the transceiver heights (the length of the metal cavity is fixed).

Figure 7c shows the simulated and measured PDPs. Similar as the previous example, only LoS and MB components exist and are considered. Parameters of the reference model are estimated as follows: $K = 2.78$, $\eta_{MB} = 1$, $N = 7$, $k_1 = 0.13$, $k_2 = 0.12$, $k_3 = 0.19$, $k_4 = 0.28$, $k_5 = 0.2$, $k_6 = 0$, and $k_7 = 0.26$. A good agreement between the simulated and measured PDP can be observed. The agreement between the simulations and measurements shown in Fig. 6b and Fig. 7c indicates that it is valid to consider the LoS propagation of generated EM fields from the excited sidewalls (sidewalls A

TABLE II
COMPARISON OF THE PARAMETERS OF THE PROPOSED MODEL AND THE FLOATING-INTERCEPT MODEL.

Scenarios	Frequency	Path Loss Exponent (γ)	Shadow Standard Deviation (σ)
LoS in empty metal cavity (PM)	300 - 312 GHz	1.987	0.017
LoS with misalignment between Tx and Rx (PM)	300 - 312 GHz	1.98	0.023
Indoor communication (FI) [24]	300 GHz	1.941	0.028
	306 GHz	1.987	0.079
	312 GHz	2.062	0.102

and C as shown in Fig. 6a) as the traveling wave bouncing back and forth between the transceivers sidewalls of the cavity.

In addition to LoS propagation, a more practical scenario with an FPGA board being put in the center of the bottom plate of the cavity was considered. Both length and width of the FPGA board are 15.2 cm and the maximum height of the board is 1.5 cm. Measurements were performed with the transceiver heights $h_t = h_r = 2.4$ cm. Figure 8a shows the measurement setup. The simulated and measured PDP are compared in Fig. 8b. For this case, Both LoS, SB, DB, and MB conditions involve in and are considered in the reference model. From the measured PDP, the parameters defined in the reference model are estimated as follows: K=3, $\eta_{SB} = \eta_{DB} = 0.1$, $\eta_{MB} = 0.8$, $N = 4$, $k_1 = 0.6$, $k_2 = 0.2$, $k_3 = k_4 = 0.1$, $R_{t1} = R_{r1} = 4.5$ cm, and $R_{t2} = R_{r2} = 26$ cm. The good match shown in Fig. 8b implies that the assumption that α_t, α_r, R_t, and R_r are uniformly distributed is reasonable. The model in [26] describes the reflection behavior of printed circuit boards (PCB) in the THz range. In contrast to model in [25], we have experimentally discovered in [17], [18] existence of resonant modes in a metal cavity at THz frequencies and proposed in this paper how to model this effect. Additionally, our paper is a general statistical model which is applicable to more possible scenarios, such as non-LoS scenario with LoS propagation being blocked by DIMM, and height-misalignment between Tx and Rx, etc.

The non-LoS (NLoS) propagation is the last scenario being considered, where a dual in-line memory module (DIMM) was put at the midpoint of the Tx - Rx link to block the LoS propagation. Measurements were performed with the transceivers' heights $h_t = h_r = 2.4$ cm. Figure 9a shows the measurement setup.

The simulated and measured PDPs are compared in Fig. 9b. Three arriving peaks shown in the measured PDP plot indicate that transmitting rays reached the Rx with three different paths. Since the LoS propagation has been blocked by the DIMM, the first peak with the excess delay of 0 ns is the consequence of the signal diffracting over the top edge of the DIMM (single bounced rays). The excess delay of the second peak which is 1.017 ns implies that the extra distance covered by the later arriving signal is 30.5 cm which is exactly the double of the distance between the Tx sidewall and the front-side of the DIMM. Therefore, it is reasonable to assume that the second peak is due to the reflections occurring on the front-side of

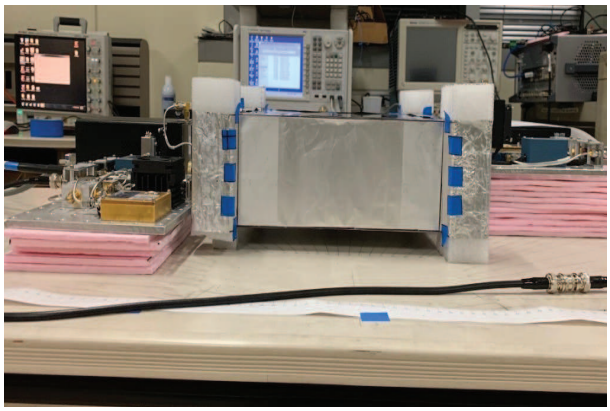

(a)

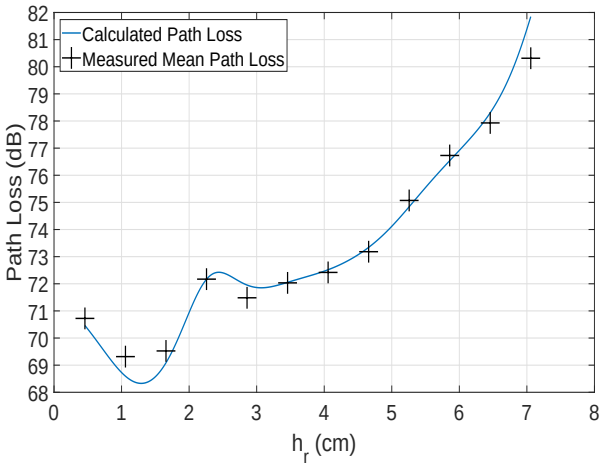

(b)

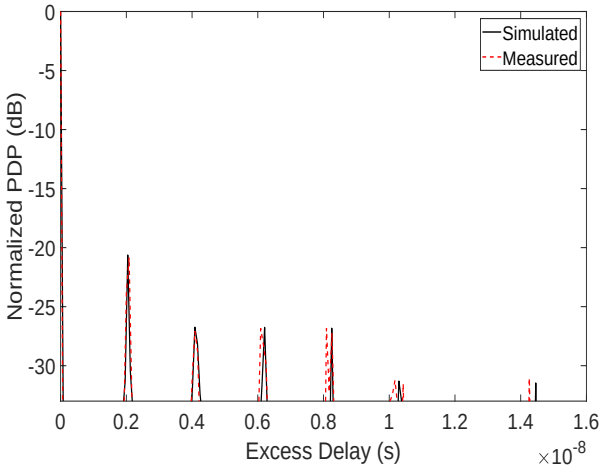

(c)

Fig. 7. LoS propagation in an empty metal cavity at 300 GHz with a misalignment between the Tx and Rx: (a) Measurement setup, (b) Comparison of the theoretical and measured path loss with respect to h_r and (c) Comparison of the normalized simulated and measured PDPs with $h_t = 2.4$ cm and $h_r = 4.8$ cm.

the DIMM and the Tx sidewall of the cavity (double-bounced rays). The third arriving peak with the excess delay of 4.087 ns arrives at the same time as the second later arriving peak of the MB component shown in the PDP plots of previous measurements. Since the LoS propagation has been blocked by the DIMM, the Ricean factor K should be set to 0. Other

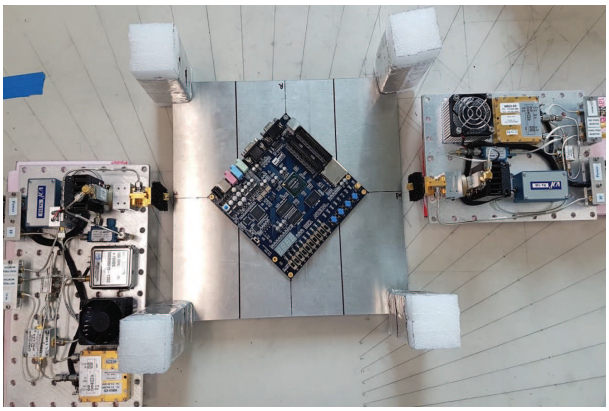

(a)

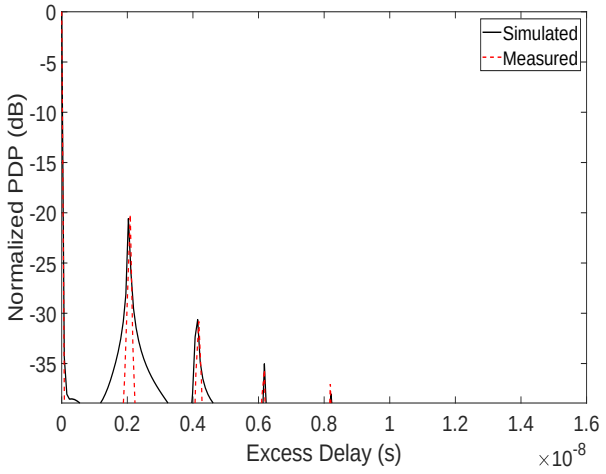

(b)

Fig. 8. LoS over an FPGA board in a metal cavity at 300 GHz with $h_t = h_r = 2.4$ cm: (a) Measurements setup and (b) Comparison of normalized theoretical and measured PDP.

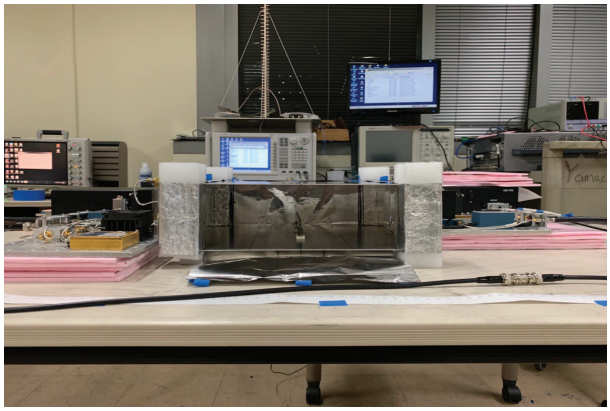

(a)

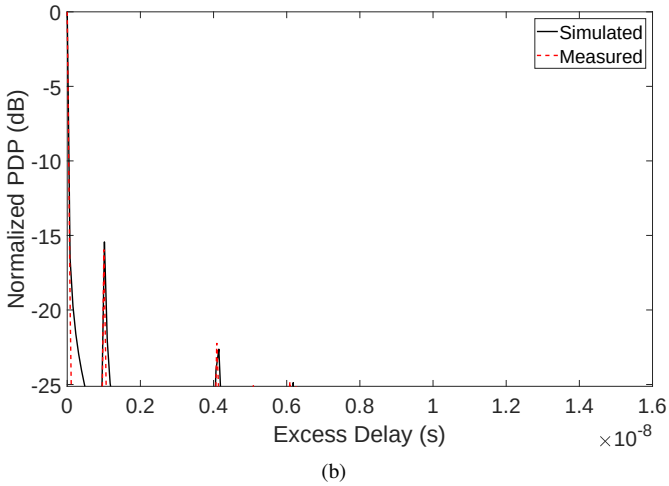

(b)

Fig. 9. The NLoS propagation in a metal cavity at 300 GHz with a DIMM as obstruction: (a) Measurements setup and (b) Comparison of the normalized theoretical and measured PDPs.

parameters of the reference model are estimated as follows: $\eta_{SB} = 0.862$, $\eta_{DB} = 0.127$, $\eta_{MB} = 0.011$, $N = 3$, $k_1 = 0.05$, $k_2 = 0.51$, $k_3 = 0.44$, $R_{t1} = 15$ cm, $R_{t2} = 15.5$ cm, $R_{r1} = 30.49$ cm, and $R_{r2} = 30.5$ cm. From Fig. 9b, a good agreement between the simulated and measured PDPs can be observed. This agreement, again, indicates that it is reasonable to simplify the modeling process by modeling the propagation of the generated EM waves as multi-bounced rays.

The parameters of the channel model for all scenarios discussed in the paper are summarized in Table III. Since the values of the parameters for the radiation pattern of the horn antenna which are $X = 0.54$, $Y = 0.45$, $Z = 11.15$, and $c = 0.01$ and are the same for all discussed scenarios, they are not listed in the table.

VII. Conclusions

This paper has proposed a two dimensional (2-D) statistical channel model for Terahertz (THz) chip-to-chip wireless communication in desktop size metal enclosures. The proposed model differs from traditional statistical channel models because it models both traveling and resonant waves that exist inside metal enclosures. Based on the cavity environment and the statistical properties of the channel inside the metal cavity, the geometrical model which describes propagation in resonant cavity as a superposition of LoS, single bounced (SB), double bounced (DB), and multi-bounced (MB) rays was proposed. Based on the geometrical model, a parametric reference model was proposed. Furthermore, the path loss model that captures signal strength variation in a resonant cavity was proposed. Frequency correlation functions (FCF) and power delay profiles (PDP) for different possible chip-to-chip communication scenarios were derived and compared with the measured PDPs. The results show a good agreement between the simulated and measured statistics.

Appendix A
Derivation of $\epsilon_r^{(j,m)}$, $\epsilon_s^{(j,m,p,q)}$, $\epsilon_s^{(m,q)}$, and $\alpha_r^{(j,m)}$

In this section, we present the derivations for the expressions shown in (3), (4), (7), and (11). We begin with the derivations of (3), and (11) with the help of a simplified geometrical model for the SB rays. As shown in Fig. 10, there are two right triangles. The sides of the blue triangle are denoted as a, b, and c. The sides of the red triangle are represented by d, e, and f. From the plot, it is observed that

$$\epsilon_r^{(j,m)} = c = \sqrt{a^2 + b^2}, \tag{48}$$

where a and b can be written as

$$a = L - R_t^j, \tag{49}$$

$$b = e - (h_r - h_t). \tag{50}$$

TABLE III
DEFINITIONS OF PARAMETERS INTRODUCED IN THE STATISTICAL GEOMETRICAL MODEL.

Parameters	Scenarios			
	LoS in empty metal cavity	LoS with a misalignment between Tx and Rx	FPGA being put on the center of the bottom plate	A DIMM being used to block the LoS propagation
h_t	2.4 cm	2.4 cm	2.4 cm	2.4 cm
h_r	2.4 cm	4.8 cm	2.4 cm	2.4 cm
K	1.55	2.78	3	0
η_{SB}	0	0	0.1	0.862
η_{DB}	0	0	0.1	0.127
η_{MB}	1	1	0.8	0.011
N	6	7	4	3
k_1	0.1667	0.13	0.6	0.05
k_2	0.1	0.12	0.2	0.51
k_3	0.1667	0.19	0.1	0.44
k_4	0.1667	0.28	0.1	0
k_5	0.2	0.2	–	–
k_6	0.2	0	–	–
k_7	–	0.26	–	–
R_{t1}	–	–	4.5 cm	15 cm
R_{t2}	–	–	26 cm	15.5 cm
R_{r1}	–	–	4.5 cm	30.49 cm
R_{r2}	–	–	26 cm	30.5 cm

e is the height of the red triangle and can be calculated with tangent function as

$$e = R_t^j tan(\alpha_t^{(j,m)}). \tag{51}$$

Using (48), (49), (50), and (51), $\epsilon_r^{(j,m)}$ can be written as

$$\epsilon_r^{(j,m)} = \sqrt{\left(L - R_t^j\right)^2 + \left(R_t^j \tan\left(\alpha_t^{(j,m)}\right) + h_t - h_c\right)^2}. \tag{52}$$

With (49), (50), and (51), $\alpha_r^{(j,m)}$ can be calculated with tangent function as

$$\alpha_r^{(j,m)} = \arctan\left(\frac{R_t^j \tan(\alpha_t^{(j,m)}) + h_t - h_r}{L - R_t^j}\right). \tag{53}$$

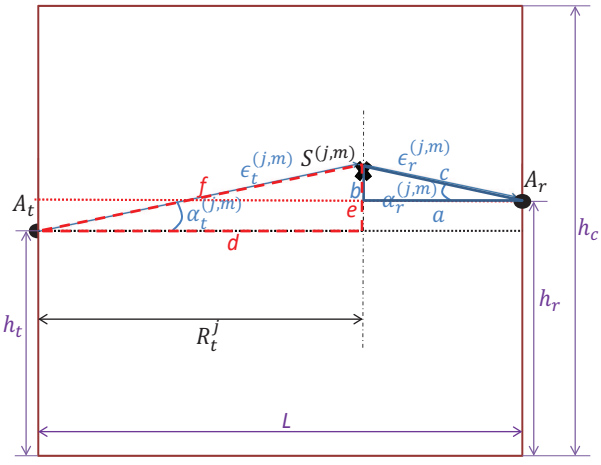

Fig. 10. The simplified geometrical model for single bounced rays.

Next, we derive (4) using a simplified geometric model for DB rays shown in Fig. 11. It is shown that there are three different triangles with the color of black, red ,and blue. The symbols a, b, and c are the three sides for the black triangle, d, e, and f are for the red triangle, and x, y, z are for the blue triangle. It can be observed from the plot that

$$\epsilon_s^{(j,m,p,q)} = c = \sqrt{a^2 + b^2}, \tag{54}$$

where a and b can be written as

$$a = R_t^j + R_r^p - L, \tag{55}$$

$$b = e + y - (h_r - h_t). \tag{56}$$

e and y represent the heights of the red and blue triangles, and can be calculated with tangent functions, respectively as

$$e = R_t^j tan\left(\alpha_t^{(j,m)}\right), \tag{57}$$

$$y = R_r^p tan\left(\alpha_r^{(p,q)}\right). \tag{58}$$

Therefore, using (54), (55), (56), (57), and (58), $\epsilon_s^{(j,m,p,q)}$ can be written as

$$\epsilon_s^{(j,m,p,q)} = \left[\left(R_t^j + R_r^p - L\right)^2 + \left(R_t^j \tan\left(\alpha_t^{(j,m)}\right) - R_r^p \tan\left(\alpha_r^{(p,q)}\right) + h_t - h_r\right)^2\right]^{\frac{1}{2}}. \tag{59}$$

Equation (4) can be derived similarly by replacing R_t^j, R_r^p with L and $\alpha_t^{j,m}$, $\alpha_r^{(p,q)}$ with α_t^m, α_r^p.

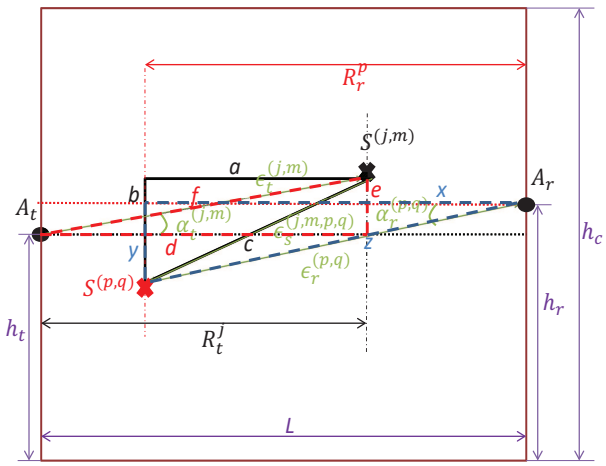

Fig. 11. The simplified geometrical model for double bounced rays.

APPENDIX B
DERIVATION OF R_{SB}, R_{DB}, AND R_{MB}

$$
\begin{aligned}
R_{SB}(\Delta f) &= \frac{E[T_{SB}(f)^* T_{SB}(f+\Delta f)]}{\Omega} \\
&= \frac{E\left[\frac{\eta_{SB}}{K+1}\frac{P_t G_t G_r}{PL_{SB}} e^{-j2\pi\Delta f \tau_{SB}}\right]}{\frac{P_t G_t G_r}{PL_{LoS}}} \\
&= \frac{\eta_{SB}}{K+1}\int_{R_{t1}}^{R_{t2}}\int_{-\theta_t}^{\theta_t}\frac{PL_{LoS}}{PL_{SB}} e^{-j2\pi\Delta f\tau_{SB}} f(R_t) f(\alpha_t) d\alpha_t dR_t \\
&= \frac{\eta_{SB}}{K+1}\int_{R_{t1}}^{R_{t2}}\int_{-\theta_t}^{\theta_t}\frac{\int_{\Delta f}\left(D_{tr}^{\frac{\gamma}{2}} f\right)^2 df}{\int_{\Delta f}\left[\left(\frac{R_t}{\cos(\alpha_t)} + \left[(L-R_t)^2 + (R_t\tan(\alpha_t)+h_t-h_r)^2\right]^{\frac{1}{2}}\right)^{\frac{\gamma}{2}} f\right]^2 df} \\
&\times \left(\frac{g(\alpha_t)\, g\left(\arctan(\frac{R_t\tan(\alpha_t)+h_t-h_r}{L-R_t})\right)}{g\left(\arctan(\frac{h_r-h_t}{L})\right) g\left(\arctan(\frac{h_t-h_r}{L})\right)}\right)^2 e^{-j2\pi\Delta f\frac{\left[(L-R_t)^2+(R_t\tan(\alpha_t)+h_t-h_c)^2\right]^{\frac{1}{2}}}{c_0}} \frac{1}{R_{t2}-R_{t1}}\frac{1}{2\theta_t} d\alpha_t dR_t.
\end{aligned} \tag{60}
$$

$$
\begin{aligned}
R_{DB}(\Delta f) &= \frac{E[T_{DB}(f)^* T_{DB}(f+\Delta f)]}{\Omega} \\
&= \frac{E\left[\frac{\eta_{DB}}{K+1}\frac{P_t G_t G_r}{PL_{DB}} e^{-j2\pi\Delta f \tau_{DB}}\right]}{\frac{P_t G_t G_r}{PL_{LoS}}} \\
&= \frac{\eta_{DB}}{K+1}\int_{R_{t1}}^{R_{t2}}\int_{R_{r1}}^{R_{r2}}\int_{-\theta_t}^{\theta_t}\int_{-\theta_r}^{\theta_r}\frac{PL_{LoS}}{PL_{DB}} e^{-j2\pi\Delta f\tau_{DB}} f(R_t) f(R_r) f(\alpha_t) f(\alpha_r) d\alpha_r d\alpha_t dR_r dR_t \\
&= \frac{\eta_{DB}}{K+1}\int_{R_{t1}}^{R_{t2}}\int_{R_{r1}}^{R_{r2}}\int_{-\theta_t}^{\theta_t}\int_{-\theta_r}^{\theta_r}\left(\frac{g(\alpha_t)g(\alpha_r)}{g\left(\arctan(\frac{h_r-h_t}{L})\right) g\left(\arctan(\frac{h_t-h_r}{L})\right)}\right)^2 \\
&\times e^{-j2\pi\Delta f\frac{\left(\frac{R_t}{\cos(\alpha_t)}+\frac{R_r}{\cos(\alpha_r)}+\left[(R_t+R_r-L)^2+(R_t\tan(\alpha_t)-R_r\tan(\alpha_r)+h_t-h_r)^2\right]^{\frac{1}{2}}\right)}{c_0}} \frac{1}{R_{t2}-R_{t1}}\frac{1}{R_{r2}-R_{r1}}\frac{1}{2\theta_t}\frac{1}{2\theta_r} \\
&\times \frac{\int_{\Delta f}\left(D_{tr}^{\frac{\gamma}{2}} f\right)^2 df}{\int_{\Delta f}\left[\left(\frac{R_t}{\cos(\alpha_t)}+\frac{R_r}{\cos(\alpha_r)}+\left[(R_t+R_r-L)^2+(R_t\tan(\alpha_t)-R_r\tan(\alpha_r)+h_t-h_r)^2\right]^{\frac{1}{2}}\right)^{\frac{\gamma}{2}} f\right]^2 df} d\alpha_r d\alpha_t dR_r dR_t.
\end{aligned} \tag{61}
$$

$$
\begin{aligned}
R_{MB}(\Delta f) &= \frac{E[T_{MB}(f)^* T_{MB}(f+\Delta f)]}{\Omega} \\
&= \frac{E\left[\frac{\eta_{SB}}{K+1}\sum_{n=1}^{N} k_n \frac{P_t G_t G_r}{PL_{MB}} e^{-j2\pi\Delta f\tau_{MB}}\right]}{\frac{P_t G_t G_r}{PL_{LoS}}} \\
&= \frac{\eta_{MB}}{K+1}\sum_{n=1}^{N}\int_{-\theta_t}^{\theta_t}\int_{-\theta_r}^{\theta_r} k_n \frac{PL_{LoS}}{PL_{MB}} e^{-j2\pi\Delta f\tau_{MB}} f(R_t) f(\alpha_t) d\alpha_r d\alpha_t \\
&= \frac{\eta_{MB}}{K+1}\int_{-\theta_t}^{\theta_t}\int_{-\theta_r}^{\theta_r} k_n \left(\frac{g(\alpha_t)\, g(\alpha_r)}{g\left(\arctan(\frac{h_r-h_t}{L})\right) g\left(\arctan(\frac{h_t-h_r}{L})\right)}\right)^2 \\
&\times e^{-j2\pi\Delta f\frac{\left(\frac{L}{\cos(\alpha_t)}+\frac{L}{\cos(\alpha_r)}+(2n-1)\int_{-\theta_t}^{\theta_t}\int_{-\theta_r}^{\theta_r}\sqrt{(L\tan(\alpha_t)-L\tan(\alpha_r)+h_t-h_r)^2+L^2}\frac{1}{2\theta_r}\frac{1}{2\theta_t}d\alpha_r d\alpha_t\right)}{c_0}} \frac{1}{2\theta_t}\frac{1}{2\theta_r} \\
&\times \frac{\int_{\Delta f}\left(D_{tr}^{\frac{\gamma}{2}} f\right)^2 df}{\int_{\Delta f}\left[\left(\frac{L}{\cos(\alpha_t)}+\frac{L}{\cos(\alpha_r)}+(2n-1)\int_{-\theta_t}^{\theta_t}\int_{-\theta_r}^{\theta_r}\sqrt{(L\tan(\alpha_t)-L\tan(\alpha_r)+h_t-h_r)^2+L^2}\frac{1}{2\theta_r}\frac{1}{2\theta_t}d\alpha_r d\alpha_t\right)^{\frac{\gamma}{2}} f\right]^2 df} d\alpha_r d\alpha_t.
\end{aligned} \tag{62}
$$

REFERENCES

[1] P. C. Jain, "Recent trends in next generation terabit ethernet and gigabit wireless local area network," in *2016 International Conference on Signal Processing and Communication (ICSC)*, Dec 2016, pp. 106–110.

[2] "IEEE draft standard for information technology–telecommunications and information exchange between systems local and metropolitan area networks–specific requirements part 11: Wireless lan medium access control (mac) and physical layer (phy) specifications–amendment: Enhanced throughput for operation in license-exempt bands above 45 GHz," *IEEE P802.11ay/D2.0, July 2018*, pp. 1–673, Jan 2018.

[3] InifiBand. (2018) Infiniband roadmap. [Online]. Available: https://www.infinibandta.org/infiniband-roadmap/

[4] T. Kürner, "THz communications: Challenges and applications beyond 100 Gbit/s," in *2018 International Topical Meeting on Microwave Photonics (MWP)*, Oct 2018, pp. 1–4.

[5] C. Cheng and A. Zajić, "Characterization of 300 GHz wireless channels for rack-to-rack communications in data centers," in *2018 IEEE 29th Annual International Symposium on Personal, Indoor and Mobile Radio Communications (PIMRC)*, Sep. 2018, pp. 194–198.

[6] N. Khalid and O. B. Akan, "Wideband THz communication channel measurements for 5G indoor wireless networks," in *Communications (ICC), 2016 IEEE International Conference on*. IEEE, 2016, pp. 1–6.

[7] S. Kim and A. G. Zajić, "Statistical characterization of 300-GHz propagation on a desktop," *IEEE Transactions on Vehicular Technology*, vol. 64, no. 8, pp. 3330–3338, 2015.

[8] S. Kim and A. Zajić, "Characterization of 300-GHz wireless channel on a computer motherboard," *IEEE Transactions on Antennas and Propagation*, vol. 64, no. 12, pp. 5411–5423, 2016.

[9] S. Priebe, C. Jastrow, M. Jacob, T. Kleine-Ostmann, T. Schrader, and T. Kürner, "Channel and propagation measurements at 300 GHz," *IEEE Transactions on Antennas and Propagation*, vol. 59, no. 5, pp. 1688–1698, 2011.

[10] S. Priebe, M. Jacob, C. Jastrow, T. Kleine-Ostmann, T. Schrader, and T. Kürner, "A comparison of indoor channel measurements and ray tracing simulations at 300 GHz," in *35th International Conference on Infrared, Millimeter, and Terahertz Waves*, Sept 2010, pp. 1–2.

[11] M. Jacob, S. Priebe, R. Dickhoff, T. Kleine-Ostmann, T. Schrader, and T. Kürner, "Diffraction in mm and sub-mm wave indoor propagation channels," *IEEE Transactions on Microwave Theory and Techniques*, vol. 60, no. 3, pp. 833–844, March 2012.

[12] T. Kleine-Ostmann, C. Jastrow, S. Priebe, M. Jacob, T. Kürner, and T. Schrader, "Measurement of channel and propagation properties at 300 GHz," in *2012 Conference on Precision electromagnetic Measurements*, July 2012, pp. 258–259.

[13] A. Fricke, S. Rey, M. Achir, P. Le Bars, T. Kleine-Ostmann, and T. Kürner, "Reflection and transmission properties of plastic materials at THz frequencies," in *2013 38th International Conference on Infrared, Millimeter, and Terahertz Waves (IRMMW-THz)*, Sep. 2013, pp. 1–2.

[14] A. Fricke, M. Achir, P. Le Bars, and T. Kürner, "Characterization of transmission scenarios for terahertz intra-device communications," in *2015 IEEE-APS Topical Conference on Antennas and Propagation in Wireless Communications (APWC)*, Sep. 2015, pp. 1137–1140.

[15] C. Cheng, S. Kim, and A. Zajić, "Study of diffraction at 30 GHz, 140 GHz, and 300 GHz," in *2018 IEEE International Symposium on Antennas and Propagation USNC/URSI National Radio Science Meeting*, July 2018, pp. 1553–1554.

[16] T. Kürner, A. Fricke, S. Rey, P. Le Bars, A. Mounir, and T. Kleine-Ostmann, "Measurements and modeling of basic propagation characteristics for intra-device communications at 60 ghz and 300 GHz," *Journal of Infrared, Millimeter, and Terahertz Waves*, vol. 36, no. 2, pp. 144–158, 2015.

[17] J. Fu, P. Juyal, and A. Zajić, "300 GHz channel characterization of chip-to-chip communication in metal enclosure," in *2019 13th European Conference on Antennas and Propagation (EuCAP)*, March 2019, pp. 1–5.

[18] ——, "THz channel characterization of chip-to-chip communication in desktop size metal enclosure," *IEEE Transactions on Antennas and Propagation*, pp. 1–1, 2019.

[19] D. He, K. Guan, A. Fricke, B. Ai, R. He, Z. Zhong, A. Kasamatsu, I. Hosako, and T. Kürner, "Stochastic channel modeling for kiosk applications in the terahertz band," *IEEE Transactions on Terahertz Science and Technology*, vol. 7, no. 5, pp. 502–513, Sep. 2017.

[20] S. Priebe and T. Kürner, "Stochastic modeling of THz indoor radio channels," *IEEE Transactions on Wireless Communications*, vol. 12, no. 9, pp. 4445–4455, Sep. 2013.

[21] S. Priebe, M. Jacob, and T. Kürner, "Angular and rms delay spread modeling in view of THz indoor communication systems," *Radio Science*, vol. 49, no. 3, pp. 242–251, March 2014.

[22] S. Kim and A. Zajić, "Statistical modeling of THz scatter channels," in *2015 9th European Conference on Antennas and Propagation (EuCAP)*, April 2015, pp. 1–5.

[23] ——, "Statistical modeling and simulation of short-range device-to-device communication channels at sub-THz frequencies," *IEEE Transactions on Wireless Communications*, vol. 15, no. 9, pp. 6423–6433, Sep. 2016.

[24] C. Cheng, S. Kim, and A. Zajić, "Comparison of path loss models for indoor 30 GHz, 140 GHz, and 300 GHz channels," in *2017 11th European Conference on Antennas and Propagation (EUCAP)*, March 2017, pp. 716–720.

[25] R. Piesiewicz, C. Jansen, D. Mittleman, T. Kleine-Ostmann, M. Koch, and T. Kürner, "Scattering analysis for the modeling of THz communication systems," *IEEE Transactions on Antennas and Propagation*, vol. 55, no. 11, pp. 3002–3009, Nov 2007.

[26] A. Fricke, T. Kürner, M. Achir, and P. L. Bars, "A model for the reflection of terahertz signals from printed circuit board surfaces," in *2017 11th European Conference on Antennas and Propagation (EUCAP)*, March 2017, pp. 711–715.

[27] S. Priebe, M. Jacob, C. Jansen, and T. Kürner, "Non-specular scattering modeling for THz propagation simulations," in *Proceedings of the 5th European Conference on Antennas and Propagation (EUCAP)*, April 2011, pp. 1–5.

[28] J. Fu, P. Juyal, and A. Zajić, "Pah loss model as function of antenna height for 300 GHz chip-to-chip communications," in *2019 IEEE International Symposium on Antennas and Propagation and USNC-URSI (APS)*. IEEE, 2019, pp. 1–2.

[29] J. Oh, A. Zajić, and M. Prvulovic, "Traffic steering between a low-latency unswitched tl ring and a high-throughput switched on-chip interconnect," in *Proceedings of the 22nd international conference on Parallel architectures and compilation techniques*. IEEE Press, 2013, pp. 309–318.

[30] J. Oh, M. Prvulovic, and A. Zajić, "Tlsync: Support for multiple fast barriers using on-chip transmission lines," in *2011 38th Annual International Symposium on Computer Architecture (ISCA)*, June 2011, pp. 105–115.

[31] A. G. Zajic, G. L. Stuber, T. G. Pratt, and S. T. Nguyen, "Wideband mimo mobile-to-mobile channels: Geometry-based statistical modeling with experimental verification," *IEEE Transactions on Vehicular Technology*, vol. 58, no. 2, pp. 517–534, Feb 2009.

[32] J. M. Jornet and I. F. Akyildiz, "Channel modeling and capacity analysis for electromagnetic wireless nanonetworks in the terahertz band," *IEEE Transactions on Wireless Communications*, vol. 10, no. 10, pp. 3211–3221, October 2011.

[33] Y. Yang, A. Shutler, and D. Grischkowsky, "Measurement of the transmission of the atmosphere from 0.2 to 2 thz," *Optics express*, vol. 19, no. 9, pp. 8830–8838, 2011.

[34] J. F. Johansson and N. D. Whyborn, "The diagonal horn as a sub-millimeter wave antenna," *IEEE Transactions on Microwave Theory and Techniques*, vol. 40, no. 5, pp. 795–800, May 1992.

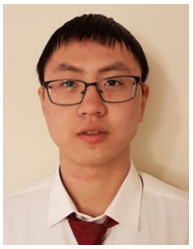

Jinbang Fu was born in Nanchang, China. In 2017, he received his B.Sc degree in Electrical and Computer Engineering with the distinction of summa cum laude from University of Massachusetts, Amherst.

Currently, he is pursuing a Ph.D degree in Electrical and Computer Engineering at Georgia Institute of Technology as a Graduate Research Assistant in the Electromagnetic Measurements in Communications and Computing Lab. His research interests include THz wireless channel measurements and modeling, and THz wireless communication system design for chip-to-chip communication.

Prateek Juyal received the B.E. degree in electronics and communication engineering from Kumaun University, Nainital, India, in 2007, M.Tech. degree in digital communication from Guru Gobind Singh Indraprastha University, Delhi, India, in 2009. He received his Ph.D. degree in electrical and computer engineering from University of Manitoba, Winnipeg, MB, Canada, in 2017.

Currently, he is working as a Posdoctoral fellow in School of Electrical and computer engineering, Georgia Institute of Technology, Atlanta, USA. His research interests include antenna design, metasurfaces application in radiating structures and THz wireless channel modeling and propagation.

Alenka Zajic (S'99–M'09–SM'13) received the B.Sc. and M.Sc. degrees form the School of Electrical Engineering, University of Belgrade, in 2001 and 2003, respectively. She received her Ph.D. degree in Electrical and Computer Engineering from the Georgia Institute of Technology in 2008. Currently, she is an Associate Professor in the School of Electrical and Computer Engineering at Georgia Institute of Technology. Prior to that, she was a visiting faculty member in the School of Computer Science at Georgia Institute of Technology, a post-doctoral fellow in the Naval Research Laboratory, and a design engineer at Skyworks Solutions Inc. Her research interests span areas of electromagnetic, wireless communications, signal processing, and computer engineering.

Dr. Zajic was the recipient of the 2017 NSF CAREER award, the Best Paper Award at MICRO 2016, 2012 Neal Shepherd Memorial Best Propagation Paper Award, the Best Student Paper Award at the IEEE International Conference on Communications and Electronics 2014, the Best Paper Award at the International Conference on Telecommunications 2008, the Best Student Paper Award at the 2007 Wireless Communications and Networking Conference, and the Dan Noble Fellowship in 2004, which was awarded by Motorola Inc. and the IEEE Vehicular Technology Society for quality impact in the area of vehicular technology.